New method for tracking the movement of ionospheric plasma

C. J. Benton[1] and C. N. Mitchell[1]

Received 17 April 2012; revised 16 August 2012; accepted 16 August 2012; published 22 September 2012.

[1] A method to track the flow of plasma in the Earth's ionosphere is presented. This takes maps of total electron content (TEC) at various times, and by comparing them derives a map of bulk velocities. The method is a modification of the Horn-Schunck scheme used in computer vision, whereby the aperture problem (caused by the scalar input field not containing enough information to uniquely constrain the vector output field) is overcome by making pragmatic assumptions about the divergence and rotation of the flow. The continuity equation linking plasma velocity and density is given source terms constrained by models of plasma generation and recombination. This can be used to mitigate solar terminator effects, where the close proximity of daytime plasma generation and nighttime recombination causes the impression of plasma flow. The method successfully reconstructs the behavior of test data. It also gives plausible results with real electron density maps from the 2003 Halloween Storms.

Citation: Benton, C. J., and C. N. Mitchell (2012), New method for tracking the movement of ionospheric plasma, *J. Geophys. Res.*, *117*, A09317, doi:10.1029/2012JA017836.

1. Introduction

[2] The electron density within the Earth's ionosphere is highly structured and constantly changing. Studying this electron density is a major topic in space weather research, as it is strongly affected by phenomena such as solar coronal mass ejections and geomagnetic disturbances [*Basu et al.*, 2001; *Doherty et al.*, 2004]. The topic is also of great practical importance, due to the effect of plasma on radio propagation. For example, Global Navigation Satellite Systems (GNSS) are affected by ionospheric plasma [*Klobuchar*, 1996]. The reduction of the group velocity of radio waves in a plasma causes spurious range measurements and so affects accuracy. More seriously, ionospheric plasma can cause rapid fluctuations in the phase or amplitude of the signal. This scintillation can cause receivers to lose lock, and in extreme cases makes GNSS completely unusable [*Skone et al.*, 2001].

[3] The movement of large regions of plasma, and in particular the extension of "tongues" of ionization has been studied [*Foster et al.*, 2005; *Middleton et al.*, 2005; *Stolle et al.*, 2006; *De Franceschi et al.*, 2007]. By observing such motion, convection phenomena, such as plasma being lifted during the 2003 Halloween Storms [*Spencer and Mitchell*, 2007] and tongues of plasma being drawn antisunward [*Middleton et al.*, 2005; *De Franceschi et al.*, 2007] have been discovered. Another reason for studying plasma motion is that moving patches [*De Franceschi et al.*, 2007; *Basu and Valladares*, 1999; *Burston et al.*, 2009] and tongues of ionization [*Kinrade et al.*, 2012] are strongly associated with scintillation, and so by tracking them, it may be possible to predict upcoming events. The idea to track high latitude plasma flow as an indication of GPS scintillation activity was proposed in *Mitchell et al.* [2005] and further substantiated in *De Francheschi et al.* [2007].

[4] Most methods for observing ionospheric electron density, such as IDA4D [*Bust et al.*, 2007] or MIDAS [*Mitchell and Spencer*, 2003] (as used below), provide no direct velocity information. This paper presents a technique to reconstruct this velocity, by comparing electron density maps at different times, and following the features. This method may seem obvious, but it has often been avoided, due to the difficulties described below. Therefore, velocity information is usually taken from models [*Alexeev et al.*, 2007] or derived from data assimilation schemes [*Bust and Crowley*, 2007; *Datta-Barua et al.*, 2009, 2011], in which compliance with models is an integral part. More specifically, this paper uses "optical flow" (or "optic flow") techniques from computer vision. Optical flow using a Kriging algorithm has been applied previously to ionospheric feature tracking [*Foster and Evans*, 2008; *Foster and Evans*, 2009; *Foster*, 2009], but in those cases it was not related to the underlying physics.

[5] Velocity is a vector quantity, and so any scheme to extract a velocity field from the scalar field of plasma density will inevitably be underdetermined. This is known as the aperture problem, after an example in which a straight moving edge is observed through a narrow aperture [*Bertero et al.*, 1988]. Regardless of the object's true direction, the resulting view is consistent with motion in many different directions.

[6] Due to the aperture problem, any useful scheme for deriving plasma velocity from density must use regularization. In other words, it must include some prior knowledge as to how probable a given solution is. A prime assumption

[1]Department of Electronic and Electrical Engineering, University of Bath, Bath, UK.

Corresponding author: C. J. Benton, Department of Electronic and Electrical Engineering, University of Bath, Claverton Down, Bath BA2 7AY, UK. (c.j.benton@bath.ac.uk)

0148-0227/12/2012JA017836

in almost all motion tracking schemes, is that the velocity at one point is likely to be similar to velocities at nearby points. There are two principal ways of doing this, namely local methods and global methods [*Bruhn et al.*, 2005]. With a local scheme, pixels in a small neighborhood are considered together. An example is the Lucas-Kanade scheme [*Lucas and Kanade*, 1981], which takes an equation describing how the image should vary with velocity and presupposes that the pixels in a neighborhood have the same velocity, giving an overdetermined set of equations from which velocity can be extracted using least squares fitting. Global schemes consider all the points together, the prime example being the Horn-Schunck method [*Horn and Schunck*, 1981]. This defines a global functional, including terms penalizing large velocity gradients, which is then minimized using the calculus of variations.

[7] An extensively modified Horn-Schunck scheme is used in this paper. The reason for choosing it over local schemes is due to what happens in the middle of features. A local scheme can only "see" what is happening within a very small area, and so it can only detect motion in the presence of an edge. Therefore, if the Lucas-Kanade method or similar is applied to a large featureless object, it will only detect motion around the object's boundaries, and report that the center of the object is motionless [*Bruhn et al.*, 2005]. Given that moving ionospheric patches usually *are* large featureless objects (at least to the resolution afforded by current imaging techniques), this would be very limiting. On the other hand, the Horn-Schunck scheme can "see" the full image, and so is capable of filling in the center of moving objects [*Bruhn et al.*, 2005].

[8] The Lucas-Kanade and Horn-Schunck techniques are known as differential techniques, which by definition take a differential equation describing how the image is expected to vary for a particular velocity field, and attempt to invert it. The word "invert" refers to this being an inverse problem, whereby the task is to extract the physical parameters of a system from observed quantities which depends on those parameters [*Tarantola*, 2005]. Differential optical flow techniques are very widely applied [*Bruhn et al.*, 2005], but other techniques exist. One such technique, which in fact has been applied to ionospheric tracking [*Foster and Evans*, 2008; *Foster*, 2009], is that of region based matching, whereby sub-blocks of maps are compared to sub-blocks of other maps shifted in all possible directions, up to a threshold value. By finding the best match, the velocity can be extracted. This is implicitly a local scheme, and like other local schemes suffers from the above filling-in problem. A further class of techniques are those based on phase [*Fleet and Jepson*, 1990; *Gautama and Van Hulle*, 2002]. It may be possible to apply such techniques to the ionosphere, but this is beyond the scope of this report. Extensive reviews of optical flow techniques have been produced by Barron, Fleet and Beauchemin [*Barron et al.*, 1994; *Beauchemin and Barron*, 1995].

[9] Another method, which has been applied to the ionosphere, is to highlight patches using a spatial filter, and then to track the position of maxima [*Burston et al.*, 2010]. This, however, can only work when clear maxima are present, and cannot reconstruct a continuous velocity field.

[10] An important issue in ionospheric tracking is the effect of plasma generation and recombination on the apparent velocity. Due to the sparse nature of the information provided, it is impossible to tell the difference between genuine motion, and phantom motion due to the recombination of plasma in one location, and the simultaneous generation of plasma in a nearby location. As with the aperture problem, the chosen solution was to incorporate knowledge about what is most probable into the reconstruction. To do this, the continuity equation, which links plasma density and velocity, was given a source term, which in most cases was regularized by minimizing its gradient. This form of regularization asserts that the above phantom motion is improbable, and so should only be considered if the velocity field resulting from the assumption of genuine plasma motion is itself improbable.

[11] The most prominent example of the generation and recombination problem occurs in the solar terminator region, whereby daytime regions in which plasma is being generated by solar irradiation are in close proximity to nighttime regions in which plasma is recombining. (The ionosphere covers a large range in altitudes, and so the solar terminator is in fact an extended boundary region, above which it may be nighttime at one point, but daytime higher up.) As the solar terminator region moves, an illusion that nearby objects are also moving is formed. In this case, the assumption of small gradients ceases to be realistic. Instead, gradients derived from a model of ionization and recombination become a more pragmatic assumption. Using such a model is not straightforward, as it must *only* calculate the source terms, and necessarily exclude the effects of transport. Attempts to construct such a model are underway, but further work is required to achieve the level of realism required to fully negate the solar terminator effects.

[12] In section 2 a novel formulation of the Horn-Schunck method, suited to tracking the flow of ionospheric plasma around the globe is developed. The resulting equations are valid in both two and three dimensions, but the focus of this paper is the two-dimensional tracking of Total Electron Content (TEC), that is the number of electrons per unit area. In section 3 a numerical method for solving the equations of the modified Horn-Schunck scheme is described. In section 4, results using both test data, and real electron density maps from the 2003 "Halloween Storms" are presented.

2. Reformulation of the Horn-Schunck Method

[13] In this section, a modified Horn-Schunck method, suited to the plasma flow problem is constructed. The derivation is done with coordinate free vector notation, allowing the resulting method to be straightforwardly adapted to flow over a sphere. Horn-Schunck variants using non-planar surfaces have been implemented before, including flow over spheres [*Imiya et al.*, 2005] and even arbitrary manifolds [*Lefèvre et al.*, 2007; *Lefèvre and Baillet*, 2008], but not as far as the authors are aware in combination with the other modifications described below. While only 2D flow is calculated in this paper, the derivation is done in 3D, as although the surface of a sphere is 2D, its intrinsic curvature is most easily represented by considering it in 3D. Therefore, the resulting equations remain valid for 3D flow.

2.1. Continuity Equation

[14] The first step is to choose an appropriate image constraint equation. This is a differential equation linking the

velocity field to the image intensity, and by inverting it, the velocity field is extracted. The equation used by Horn and Schunck, and widely used elsewhere [*Beauchemin and Barron*, 1995], is

$$\vec{v} \cdot \nabla I = -\frac{\partial I}{\partial t} \tag{1}$$

where t is time, $\vec{v}$ is the velocity field, and I is the image intensity field, a quantity usually proportional to image brightness. If the image intensity field is to be replaced with plasma density ρ, then the image constraint equation should be replaced with the continuity equation

$$\nabla \cdot (\rho \vec{v}) + \frac{\partial \rho}{\partial t} = s \tag{2}$$

which gives a more natural description of how density relates to velocity. A particular difference between the two is that equation (1) is symmetric under the transformation $I \rightarrow c - I$, for arbitrary constant c, which means that the method will interpret a dark feature moving against a light background in exactly the same way as a light feature against a dark background. This is inappropriate for tracking plasma flow, as a bubble of low electron density moving through a region of higher electron density will be interpreted as moving into a particular location, when in fact plasma is moving *out* of that location.

[15] The different maps of plasma density enter the continuity equation via the terms ρ and $\partial\rho/\partial t$. There are various ways of combining the map data into these values. The method chosen in this paper it assign the mean values of the two maps being compared to ρ, and the difference between the maps to $\partial\rho/\partial t$. This definition sets the unit of time to the time interval between maps. Other methods include assigning just one of the maps to ρ, or using a three-map scheme, where ρ is taken from the central map, and $\partial\rho/\partial t$ is derived from the maps on either side. These alternatives were found to make remarkably little difference to the calculated velocity field.

[16] The continuity equation includes a source term s, equal to the rate of ionization per unit volume, minus the rate of recombination per unit volume. Like $\vec{v}$, this must also be derived from the inversion, and be subject to regularization, as is described in section 2.3. Modified Horn Schunck terms using the continuity equation have been implemented before [*Wildes et al.*, 2000; *Corpetti et al.*, 2002, 2006], but not with source terms, and not with the other modifications described here.

2.2. Velocity Smoothness Regularization

[17] The second step is to implement the assumption that the velocity at one point is likely to be similar to velocities at nearby points. The Horn-Schunck method applies this assumption by defining a regularization term, which is later integrated over space, forming a functional. This functional, together with other terms, will then be minimized using the calculus of variations. The Horn-Schunck scheme uses a regularization term of the form

$$R'_v = \gamma\left(|\nabla \cdot \vec{v}|^2 + |\nabla \times \vec{v}|^2\right) \tag{3}$$

This in fact differs from the expression used in the original Horn-Schunck paper, but the change has little effect, due to both forms giving the same result when minimized using the Euler Lagrange equations [*Corpetti et al.*, 2006]. The first reason for this change in formulation is that Horn and Schunck's original term applied gradient operators separately to the Cartesian components of the velocity field, an operation which is equivalent to the covariant derivative. This is straightforward on the planar surface that Horn and Schunck used, but in the general case, tensor calculus is required [*Lefèvre et al.*, 2007; *Lefèvre and Baillet*, 2008]. Changing to this new term simplifies the analysis, by allowing vector calculus to be used instead.

[18] The second reason for the change in formulation is that it highlights the assumptions being made by the regularization. From a physical point of view, the regularization defined by equation (3) implies that divergenceless irrotational flow, also known as Laplacian flow, is most probable, and that any deviation from this assumption requires evidence to the contrary. This is a pragmatic assumption when the source term s is uniform, but non-uniform generation will naturally result in non-zero divergence, as plasma diffuses out of or in to regions of higher or lower generation. Therefore, a more appropriate target for minimization is a modified divergence term, in which an estimate of the divergence due to inhomogeneous s is treated as the default solution. This can be estimated by considering the influence of uneven s on a uniform plasma with density $\rho = \bar{\rho}$. Rearranging the continuity equation gives

$$\vec{v} \cdot \nabla \rho + \rho \nabla \cdot \vec{v} + \frac{\partial \rho}{\partial t} = s \tag{4}$$

In one extreme, the uniformity of the plasma density is maintained by rapid flow to or from regions where s differs from its mean $\bar{s}$. In such a case $\partial\bar{\rho}/\partial t = \bar{s}$ and $\nabla\bar{\rho} = 0$ and so

$$\nabla \cdot \vec{v} = \frac{s - \bar{s}}{\bar{\rho}} \tag{5}$$

At the other extreme, the plasma simply stays where it is, such that

$$\nabla \cdot \vec{v} = 0 \tag{6}$$

Interpolating between these cases, something of the magnitude

$$\nabla \cdot \vec{v} = r_d \frac{s - \bar{s}}{\bar{\rho}} \tag{7}$$

is probable. The divergence correction parameter r_d ranges from 0, which corresponds to no correction to the divergence, to 1, which corresponds to a maximum correction, whereby local deviations in s cause immediate inflow or outflow. This allows a modified regularization term

$$R_v = r_v^2 \left[\left(\nabla \cdot \vec{v} - r_d \frac{s - \bar{s}}{\bar{\rho}} \right)^2 + |\nabla \times \vec{v}|^2 \right] \tag{8}$$

to be constructed, where the r_v coefficient defines the extent to which deviations from zero rotation and the expected divergence are penalized. Another potential modification, but one beyond the scope of this paper, is to apply different coefficients to the divergence and curl part of the regularization term [*Suter*, 1994].

2.3. Generation and Recombination Regularization

[19] The third step is to add a model of plasma generation and recombination into the model. As with the velocity regularization, the aim of this is not to force a particular value, but to assert it as the most pragmatic assumption, allowing deviations from the model to be made if other evidence points to the contrary. Therefore, a regularization term, again to be integrated over space and minimized, of the form

$$R_s = r_s^2 (s - s_{\mathrm{m}})^2 \tag{9}$$

is used, where s is the net generation and recombination rate actually adopted, and s_{m} is a model for s. The coefficient r_s defines how much deviations from the model are penalized.

[20] It will become apparent in section 2.5 that this regularization term amounts to a restriction on the gradient of s, rather than its direct value. Therefore, the generation and recombination regularization is in fact promoting a particular gradient field as being the most probable. In particular, when away from the solar terminator region, s_{m} can be set to zero, which promotes the assumption that small gradients in s are most probable. This corresponds to the assumption mentioned in the introduction, of phantom plasma motion being generally less likely than real motion.

[21] When close to the solar terminator region, a model promoting non-zero gradients will be required. In practice, only a model of the F-region is required, as this contains the bulk of the plasma visible using imaging techniques such as MIDAS. Most ionospheric models are unsuitable for this purpose, as they provide the rate of change of the electron density $\partial\rho/\partial t$, which by the continuity equation (equation (2)) is the sum of both the required source term s and an unwanted transport term $-\nabla \cdot (\rho\vec{v})$. There is no straightforward way of separating the source and transport terms, as they both represent multiple complex phenomena. The source term has contributions from solar photoionization, ionization by energetic particles, and recombination, while the transport term has contribution from thermal expansion, neutral winds, electric fields and diffusion [*Rishbeth*, 1986]. Therefore a customized model is required, an example of which is given in Appendix A.

2.4. Energy Functional

[22] Now that the image constraint equation, the velocity regularization term, and the generation recombination regularization term have been defined, they can be combined into an energy functional, which when minimized will balance the various demands being made on the velocity field, and return a compromise solution. The continuity equation itself is implemented by penalizing deviation from the term

$$C = \left(\nabla \cdot (\rho\vec{v}) + \frac{\partial \rho}{\partial t} - s \right)^2 \tag{10}$$

Putting everything together, and integrating over all space $\mathcal{S}$ gives the functional

$$E = \int_{\mathcal{S}} L \mathrm{d}\mathcal{S} \tag{11}$$

where the combined integrand $L = C + R_v + R_s$ is given by

$$L = \left(\nabla \cdot (\rho\vec{v}) + \frac{\partial \rho}{\partial t} - s \right)^2 + r_v^2 \left[\left(\nabla \cdot \vec{v} - r_d \frac{s - \bar{s}}{\bar{\rho}} \right)^2 + |\nabla \times \vec{v}|^2 \right] + r_s^2 (s - s_{\mathrm{m}})^2 \tag{12}$$

Minimizing equation (11) in $\vec{v}$ will yield the velocity field.

2.5. Euler Lagrange Equations

[23] A functional such as equation (11) can be minimized by applying the Euler Lagrange equations to the integrand. This is a slightly unusual case, as the integrand contains a vector quantity. However, if the Cartesian components of the vector are treated as separate functions, a separate Euler Lagrange equation can be calculated for each component, and these recombined into a vector equation. All of the vector operations in equation (12) are coordinate independent, and so a result derived in one coordinate system is valid in the general case.

[24] The Euler Lagrange equations for the components of $\vec{v}$ are

$$\frac{\partial L}{\partial v_x} - \frac{\partial}{\partial x}\frac{\partial L}{\partial\left(\frac{\partial v_x}{\partial x}\right)} - \frac{\partial}{\partial y}\frac{\partial L}{\partial\left(\frac{\partial v_x}{\partial y}\right)} - \frac{\partial}{\partial z}\frac{\partial L}{\partial\left(\frac{\partial v_x}{\partial z}\right)} = 0 \tag{13}$$

$$\frac{\partial L}{\partial v_y} - \frac{\partial}{\partial y}\frac{\partial L}{\partial\left(\frac{\partial v_y}{\partial x}\right)} - \frac{\partial}{\partial y}\frac{\partial L}{\partial\left(\frac{\partial v_y}{\partial y}\right)} - \frac{\partial}{\partial z}\frac{\partial L}{\partial\left(\frac{\partial v_y}{\partial z}\right)} = 0 \tag{14}$$

$$\frac{\partial L}{\partial v_z} - \frac{\partial}{\partial z}\frac{\partial L}{\partial\left(\frac{\partial v_z}{\partial x}\right)} - \frac{\partial}{\partial y}\frac{\partial L}{\partial\left(\frac{\partial v_z}{\partial y}\right)} - \frac{\partial}{\partial z}\frac{\partial L}{\partial\left(\frac{\partial v_z}{\partial z}\right)} = 0 \tag{15}$$

which after substitution with equation (12) and recombination into vectors gives

$$\rho\nabla\left(\nabla \cdot (\rho\vec{v}) + \frac{\partial \rho}{\partial t} \right) - \left(\rho + \frac{r_d r_v^2}{\bar{\rho}} \right)\nabla s + r_v^2 \nabla^2 \vec{v} = 0 \tag{16}$$

The Euler Lagrange equation for s reduces to $\partial L/\partial s = 0$, which gives

$$\left(1 + r_s^2 + \frac{r_d^2 r_v^2}{\bar{\rho}^2} \right) s - \left(\nabla \cdot (\rho\vec{v}) + \frac{\partial \rho}{\partial t} + \frac{r_d r_v^2}{\bar{\rho}} \nabla \cdot \vec{v} + r_s^2 s_{\mathrm{m}} + \frac{r_d^2 r_v^2}{\bar{\rho}^2} \bar{s} \right) = 0 \tag{17}$$

Rearranging gives

$$\nabla^2 \vec{v} = \left(\frac{\rho}{r_v^2} + \frac{r_d}{\bar{\rho}} \right)\nabla s - \frac{\rho}{r_v^2}\nabla\left(\rho \nabla \cdot \vec{v} + \vec{v} \cdot \nabla \rho + \frac{\partial \rho}{\partial t} \right) \tag{18}$$

$$\nabla s = \frac{1}{r_s^2 + \frac{r_d^2 r_v^2}{\bar{\rho}^2}} \nabla\left(\frac{r_d r_v^2}{\bar{\rho}} \nabla \cdot \vec{v} + r_s^2 s_{\mathrm{m}} \right) \tag{19}$$

where equation (19) has been simplified by canceling out a set of terms which together form the continuity equation.

[25] It can be seen that s_{m} only enters equation (19) via its gradient. This gives the result mentioned in section 2.3, where the generation and recombination regularization is in fact a restriction on these quantity's spatial gradients, rather than their direct values.

[26] Equations (18) and (19) can be combined by eliminating s, giving

$$\nabla^2\vec{v} = \vec{f}(\vec{v}) \tag{20}$$

where the operator $\vec{f}$ is defined as

$$\vec{f}(\vec{v}) = \frac{\bar{\rho}^2\rho + r_v^2\bar{\rho}r_d}{r_v^2\bar{\rho}^2r_s^2 + r_d^2r_v^4}\nabla\left(\frac{r_dr_v^2}{\bar{\rho}}\nabla\cdot\vec{v} + r_s^2s_{\mathrm{m}}\right) - \frac{\rho}{r_v^2}\nabla\left(\rho\nabla\cdot\vec{v} + \vec{v}\cdot\nabla\rho + \frac{\partial\rho}{\partial t}\right) \tag{21}$$

Solving equation (20) will give the velocity field. A method to do so is presented in section 3.

3. Numerical Method

[27] In this section an appropriate reformulation of the numerical method used in the original Horn-Schunck paper is derived. This can be used to track TEC around the globe. In brief, the Laplacian operator in equation (20) is represented using matrix convolution, allowing the equation to be rearranged into one representing an iterative scheme. This can be used to gradually refine an estimate for the velocity field into a real solution.

3.1. Matrix Convolution Formulation

[28] On a unit sphere, the vector Laplacian is given by [*Benyu and Weiming*, 1995]

$$\nabla^2\vec{v} = \left(\frac{1}{\cos^2\theta}\frac{\partial^2v_\lambda}{\partial\lambda^2} + \frac{\partial^2v_\lambda}{\partial\theta^2} - \frac{\sin\theta}{\cos\theta}\frac{\partial v_\lambda}{\partial\theta} - \frac{v_\lambda}{\cos^2\theta} - \frac{2\sin\theta}{\cos^2\theta}\frac{\partial v_\theta}{\partial\lambda}\right)\vec{\lambda} + \left(\frac{1}{\cos^2\theta}\frac{\partial^2v_\theta}{\partial\lambda^2} + \frac{\partial^2v_\theta}{\partial\theta^2} - \frac{\sin\theta}{\cos\theta}\frac{\partial v_\theta}{\partial\theta} - \frac{v_\theta}{\cos^2\theta} + \frac{2\sin\theta}{\cos^2\theta}\frac{\partial v_\lambda}{\partial\lambda}\right)\vec{\theta} \tag{22}$$

where λ is longitude and θ is latitude. Using a unit sphere amounts to using Earth-radii as the unit of distance, which in turn sets the unit of velocity to Earth-radii per time interval between maps. The unit vectors $\vec{a}$ and $\vec{\theta}$ are tangential to the surface, and point along lines of longitude and latitude respectively. Equation (22) can be factorized to give

$$\nabla^2\vec{v} = \left(\tilde{A}v_\lambda - \tilde{B}v_\theta\right)\rightarrow\lambda + \left(\tilde{B}v_\lambda + \tilde{A}v_\theta\right)\vec{\theta} \tag{23}$$

Where the operators $\tilde{A}$ and $\tilde{B}$ are defined as

$$\tilde{A} \equiv \left(\frac{1}{\cos^2\theta}\frac{\partial^2}{\partial\lambda^2} + \frac{\partial^2}{\partial\theta^2} - \frac{\sin\theta}{\cos\theta}\frac{\partial}{\partial\theta} - \frac{1}{\cos^2\theta}\right) \tag{24}$$

$$\tilde{B} \equiv \left(\frac{2\sin\theta}{\cos^2\theta}\frac{\partial}{\partial\lambda}\right) \tag{25}$$

The next step is to represent the velocity components v_λ and v_θ with matrices, in which case the operators $\tilde{A}$ and $\tilde{B}$ can be represented as 3×3 convolution matrices $\hat{A}$ and $\hat{B}$, such that

$$\tilde{A}v_{\lambda,\theta} \rightarrow \hat{A} * \hat{v}_{\lambda,\theta} \tag{26}$$

$$\tilde{B}v_{\lambda,\theta} \rightarrow \hat{B} * \hat{v}_{\lambda,\theta} \tag{27}$$

where the matrices are defined so that the vertical index varies in θ and the horizontal index varies in λ. The convolution operation is defined to be cyclic in the λ direction, and reflective of the element shifted horizontally by half the matrix's width in the θ direction. The first of these conditions amounts to defining the consequence of crossing the 180° meridian, while the latter describes the consequence of crossing the north or south pole. In actual fact, the boundary conditions at the poles become irrelevant, due to the numerical problem described below. Suitable components for $\hat{A}$ and $\hat{B}$ can be derived by using finite difference formulae for the derivatives

$$\frac{dv_{\lambda,\theta}}{dx} \approx \frac{v_{\lambda,\theta}(x+h) - v_{\lambda,\theta}(x-h)}{2h} \tag{28}$$

$$\frac{d^2v_{\lambda,\theta}}{dx^2} \approx \frac{v_{\lambda,\theta}(x+h) - 2v_{\lambda,\theta}(x) + v_{\lambda,\theta}(x-h)}{h^2} \tag{29}$$

where x is the independent variable, and h is the step size between adjacent elements in the v_λ and v_θ matrices. This gives

$$\hat{A} \equiv \begin{bmatrix} 0 & \left(\frac{1}{h^2} + \frac{\sin\theta}{2h\cos\theta}\right) & 0 \\ \frac{1}{h^2\cos^2\theta} & -\left(\frac{1}{\cos\theta} + \frac{2}{h^2} + \frac{2}{h^2\cos^2\theta}\right) & \frac{1}{h^2\cos^2\theta} \\ 0 & \left(\frac{1}{h^2} - \frac{\sin\theta}{2h\cos\theta}\right) & 0 \end{bmatrix} \tag{30}$$

$$\hat{B} \equiv \begin{bmatrix} 0 & 0 & 0 \\ -\frac{\sin\theta}{h\cos^2\theta} & 0 & \frac{\sin\theta}{h\cos^2\theta} \\ 0 & 0 & 0 \end{bmatrix} \tag{31}$$

Writing equation (20) in this form gives

$$\hat{A} * v_\lambda - \hat{B} * v_\theta = f_\lambda(v_\lambda, v_\theta) \tag{32}$$

$$\hat{A} * v_\theta + \hat{B} * v_\lambda = f_\theta(v_\lambda, v_\theta) \tag{33}$$

where $f_\lambda(v_\lambda, v_\theta) \equiv \vec{\lambda}\cdot\vec{f}$ and $f_\theta(v_\lambda, v_\theta) \equiv \vec{\theta}\cdot\vec{f}$ are the tangential vector components of equation (21).

3.2. Iterative Solution

[29] In the form of equations (32) and (33), the Euler Lagrange equations can be solved using an iterative scheme, which takes an estimate for v_λ and v_θ, and returns a refined estimate. The first step is to separate out the central elements of the convolution matrices, so that

$$\hat{A} * x = \hat{A}' * x + ax \tag{34}$$

$$\hat{B} * x = \hat{B}' * x + bx \tag{35}$$

where $\hat{A}'$ and $\hat{B}'$ are matrices with zero central element, and a and b are the removed central components. For the finite difference scheme used, the central component of $\hat{B}$ is

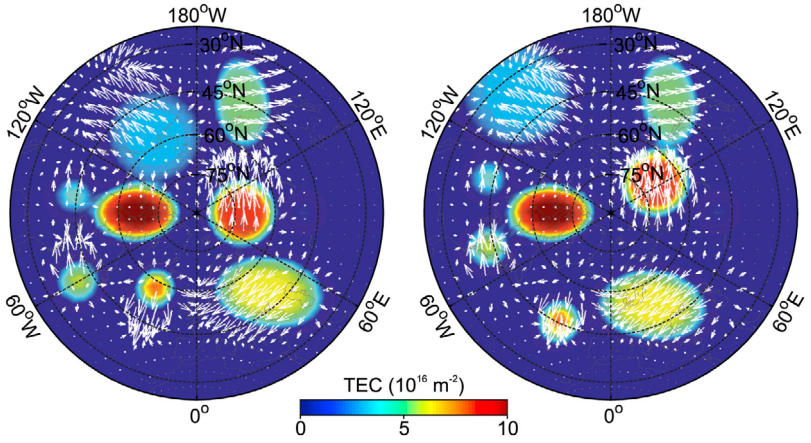

Figure 1. Application of the method to movement of test objects: (left) the first map and (right) the second map. All of the objects move, except for the large blob to left of center, and the faint blob to the far right. The calculated velocity arrows are the same for both maps. Regularization parameters $r_v = 0.15$, $r_s = 0.5$ and $r_d = 0$ are used.

already zero, making the isolation of b strictly-speaking unnecessary. However, to emphasize the method being employed, the general case is shown. This gives

$$\hat{A}' \equiv \begin{bmatrix} 0 & \left(\frac{1}{h^2} + \frac{\sin\theta}{2h\cos\theta}\right) & 0 \\ \frac{1}{h^2\cos^2\theta} & 0 & \frac{1}{h^2\cos^2\theta} \\ 0 & \left(\frac{1}{h^2} - \frac{\sin\theta}{2h\cos\theta}\right) & 0 \end{bmatrix} \tag{36}$$

$$\hat{B}' \equiv \begin{bmatrix} 0 & 0 & 0 \\ -\frac{\sin\theta}{h\cos^2\theta} & 0 & \frac{\sin\theta}{h\cos^2\theta} \\ 0 & 0 & 0 \end{bmatrix} \tag{37}$$

and

$$a = -\left(\frac{1}{\cos\theta} + \frac{2}{h^2} + \frac{2}{h^2\cos^2\theta}\right) \tag{38}$$

$$b = 0 \tag{39}$$

Applying this separation of $\hat{A}$ and $\hat{B}$ to equations (32) and (33) gives

$$\hat{A}' * v_\lambda - \left(\frac{1}{\cos\theta} + \frac{2}{h^2} + \frac{2}{h^2\cos^2\theta}\right) v_\lambda - \hat{B}' * v_\theta = f_\lambda(v_\lambda, v_\theta) \tag{40}$$

$$f_\theta(v_\lambda, v_\theta)\hat{A}' * v_\theta - \left(\frac{1}{\cos\theta} + \frac{2}{h^2} + \frac{2}{h^2\cos^2\theta}\right) v_\theta + \hat{B}' * v_\lambda = f_\theta(v_\lambda, v_\theta) \tag{41}$$

Rearranging gives

$$v_\lambda = \frac{h^2\cos^2\theta}{h^2\cos\theta + 2\cos^2\theta + 2}\left(\hat{A}' * v_\lambda - \hat{B}' * v_\theta - f_\lambda(v_\lambda, v_\theta)\right) \tag{42}$$

$$v_\theta = \frac{h^2\cos^2\theta}{h^2\cos\theta + 2\cos^2\theta + 2}\left(\hat{A}' * v_\theta + \hat{B}' * v_\lambda - f_\theta(v_\lambda, v_\theta)\right) \tag{43}$$

which is the desired iterative scheme. The functions $f_\lambda(v_\lambda, v_\theta)$ and $f_\theta(v_\lambda, v_\theta)$ contain vector differential operators, but as only a forward calculation is required, they can readily be evaluated using the above finite difference formulae.

[30] By starting with an estimate of v_λ and v_θ, a better estimate can be obtained. This starting estimate will have no effect on the final solution, and so for simplicity, a uniform set of zeros was chosen. This can be fed back into the equations, yielding a better estimate, and so on, until the method converges upon a stable solution.

3.3. Numerical Implementation of Iterative Scheme

[31] The iterative method was written in Matlab. The convergence of the iterative scheme was somewhat temperamental, but with suitable choices of regularization parameters, it could be made to converge. To stabilize the scheme, instead of each old estimate being replaced with the new estimate, it was replaced with a weighted average, containing about 1% of the new estimate. This required many more iterations, but greatly increased the numerical stability.

[32] It was also found that after stabilizing on a solution, the scheme would after a few tens or hundreds of iterations start to diverge, possibly due to numerical noise being somehow reinforced. Therefore a metric of convergence, equivalent to the root-mean square of the change in velocity was calculated at each iteration. By observing this metric over a typical run, it could be seen that after an initial period of quasi-random variation, the value decreased steadily until the solution was reached, before increasing again with the onset of numerical instability. Therefore, after a small number of mandatory iterations, to account for the quasi-random initial behavior, the scheme was stopped when the convergence metric reached a local minimum.

[33] Another issue with the numerical implementation is that toward the poles, the $1/\cos(\theta)$ factors within the vector Laplacian diverge to infinity. As polar regions are often of particular interest, it is useful to rotate the coordinate system, so that the mathematical poles lie at uninteresting geographical locations, where a distortion of the results is not a great problem. Such locations are easy to come by, as accurate TEC data is usually not available over the middle

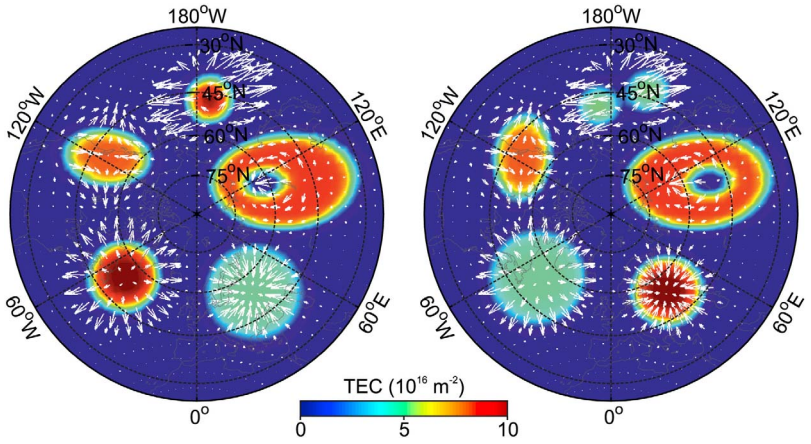

Figure 2. Application of the method to various plasma-conserving deformations of test objects: (left) the first map and (right) the second map. The calculated velocity arrows are the same for both maps. Clockwise from top: Object fission, movement of internal bubble, contraction, expansion, and reshaping. Regularization parameters $r_v = 0.15$, $r_s = 0.5$ and $r_d = 0$ are used.

of oceans or over large sparsely populated regions. To prevent infinities from entering the numerical scheme, a maximum pseudolatitude in this rotated system was defined, beyond which the magnitude of $1/\cos(\theta)$ was allowed to go no higher.

4. Results

4.1. Reconstructions Using Test Structures

[34] Test data were prepared to determine how the method coped with various phenomena. The test shown in Figure 1 concerns pure movement. A variety of test objects were drawn on a pair of maps, with varying translations between the two. Despite a relatively dense field of objects moving in different directions, the individual motion of each object was successfully reconstructed. Stationary objects were correctly reported as not moving. Furthermore, the velocity fields within the centers of featureless objects were correctly filled in, rather than motion only being detected at edges.

[35] The test shown in Figure 2 applies the method to objects undergoing various forms of plasma-conserving deformation. In all cases, physically reasonable accounts of the plasma flow were deduced. This is most noteworthy in the case of an internal bubble being moved within a larger object; the method correctly interprets the feature as a region that plasma flows out of, rather than naively following the apparent movement.

[36] The test shown in Figure 3 applies the method to various forms of plasma generation and recombination. This is a more challenging problem, as the method must deduce both velocity and net generation, and even qualitatively, there is no single correct answer. However, in all cases, perfectly plausible reconstructions of the velocity are given. In most of these cases, the plasma generation or recombination was interpreted as having a wider spatial extent than the appearing or disappearing object, with the difference accounted for by an inrush or outrush of plasma. This is a consequence of the generation and recombination regularization, which has the effect of smoothing out sharp features in *s*.

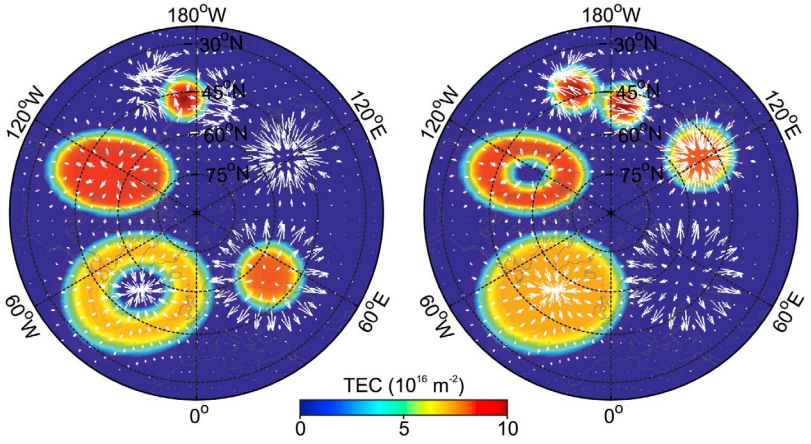

Figure 3. Application of the method to various forms of plasma generation and recombination: (left) the first map and (right) the second map. The calculated velocity arrows are the same for both maps. Clockwise from top: Object duplication, object creation, object disappearance, bubble removal, and bubble formation. Regularization parameters $r_v = 0.15$, $r_s = 0.5$ and $r_d = 0.5$ are used.

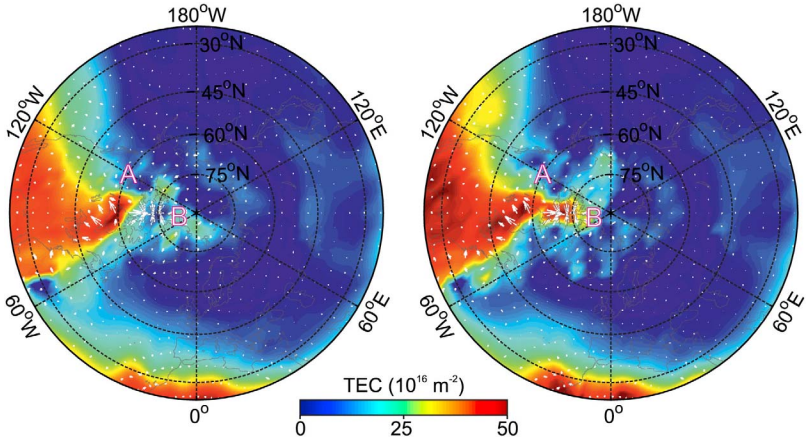

Figure 4. Application of method to flow of plasma during the Halloween Storms showing (left) TEC at 16:45 UTC on October 30th 2003 and (right) TEC at 17:15 UTC. The arrows are the same on both plots, and show the reconstructed flow of plasma. They have been extended for clarity. Note, as described in the text, the large patch moving south-west over Hudson Bay (A), and another patch appearing to the north of this (B). Regularization parameters $r_v = 0.15$, $r_s = 0.5$ and $r_d = 0.5$ are used.

4.2. Reconstruction Using Real Ionospheric Data

[37] The Halloween storms were a period of extreme solar activity, lasting from late October to early November 2003, during which multiple X-class (the most powerful class) solar flares were observed. On October 28th 2003, a colossal X-17 class flare occurred, followed by an X-7 flare on the 29th [*Tsurutani et al.*, 2005]. These caused extreme ionospheric disturbances, which peaked on the 30th [*Mannucci et al.*, 2005]. Patches of plasma were seen to move through the ionosphere, and the physics behind this movement has been extensively studied [e.g., *Mitchell et al.*, 2005; *Stolle et al.*, 2006; *De Franceschi et al.*, 2007; *Spencer and Mitchell*, 2007].

[38] Tomographic maps, showing these structures were prepared using the MIDAS tomographic algorithm [*Mitchell and Spencer*, 2003]. This uses measurements from dual frequency GPS receivers, located around the globe. By measuring the phase differences between the 1575.42 MHz L1 signal, and the 1227.60 MHz L2 signal, the line integral of electron density between the satellite and receiver can be calculated. Tomographic algorithms are then used to calculate the 3D distribution of electron density, which can then be integrated vertically to provide TEC. We created maps using data from a range of sources, as listed in the acknowledgments.

[39] In order to preserve the integrity of the reconstruction over the north pole, the coordinate system was rotated so that coordinate poles were located on the equator. Examples of plasma tracking is shown in Figures 4, 5 and 6. In all cases the moving patches were either far away from the solar terminator region, or close enough to the pole to minimize diurnal variation, thus allowing $s_m = 0$ to be used.

[40] In Figure 4, a large patch over Hudson Bay moves south-westward, and is successfully tracked doing so. Another patch appears to the north, which is interpreted as

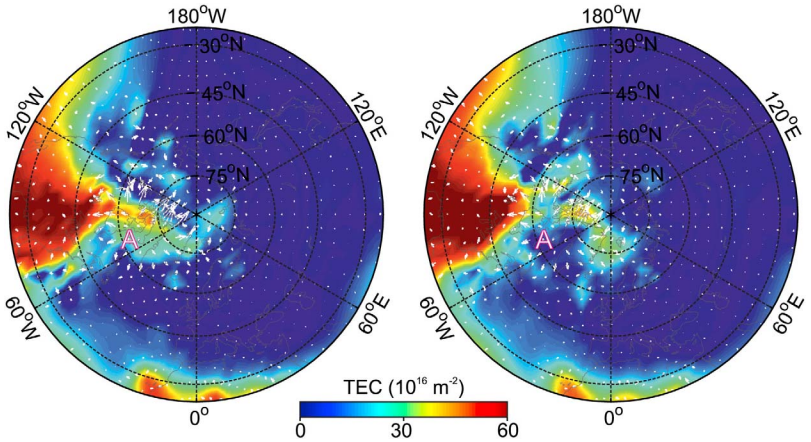

Figure 5. Application of method to flow of plasma during the Halloween Storms showing (left) TEC at 18:00 UTC on October 30th 2003 and (right) TEC at 18:30 UTC. The arrows are the same on both plots, and show the reconstructed flow of plasma. They have been extended for clarity. Note, as described in the text, the large patch between Greenland and Canada breaking up (A). Regularization parameters $r_v = 0.15$, $r_s = 0.5$ and $r_d = 0.5$ are used.

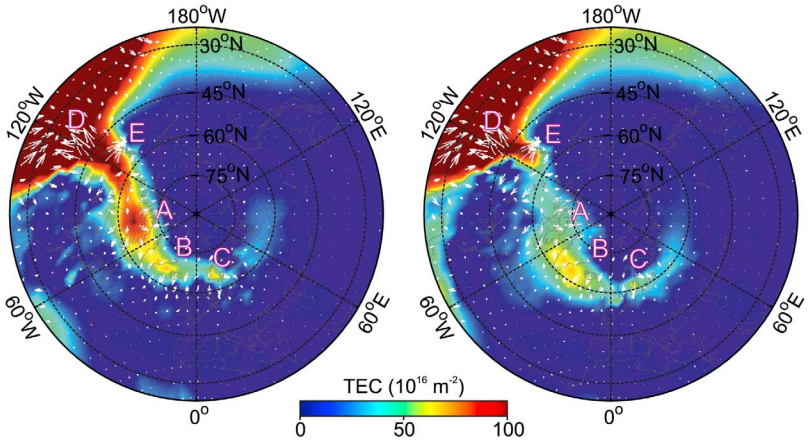

Figure 6. Application of method to flow of plasma during the Halloween Storms showing (left) TEC at 21:45 UTC on October 30th 2003 and (right) TEC at 22:15 UTC. The arrows are the same on both plots, and show the reconstructed flow of plasma. They have been extended for clarity. Note, as described in the text, the dissipation of a patch between Hudson Bay and Baffin Island (A), a patch between Greenland and Iceland moving south (B), another patch over Scandinavia moving south (C), a very large region over the USA and Pacific Ocean retreating south (D), and a protuberance from this over Vancouver moving west (E). Regularization parameters $r_v = 0.15$, $r_s = 0.5$ and $r_d = 0.5$ are used.

inrush from surrounding regions, but it may in fact be particle precipitation. In Figure 5, a large patch between Greenland and Canada is seen to break up into fragments, with the outflow being tracked. In Figure 6, a patch between Hudson Bay and Baffin Island dissipates, an event which is interpreted as outrush from the previous location. A patch between Greenland and Iceland moves south, as does another patch over Scandinavia, with the movement being tracked in both cases. Similarly, a very large region over the USA and Pacific Ocean is tracked retreating south, with a protuberance from this over Vancouver being tracked moving west.

4.3. Reconstructions on Simulated Solar Terminator Region

[41] The tests shown in Figures 7 and 8 apply the method to objects straddling a simulated solar terminator region. A simple model of the ionosphere, as outlined in Appendix A was used to construct the maps. Test objects, both moving southwards were superimposed on the solar terminator region. Figure 7 shows the result of a velocity reconstruction without any generation and recombination model being used. This causes an apparent plasma flow into the sunlit region, which distorts the apparent direction of motion for each object. In Figure 7, a generation and recombination model is added, thus providing the correct direction. This example is somewhat contrived, as the same model is used to both add the sunrise, and to compensate for it in the reconstruction. However, it demonstrates the basic principle to be valid.

4.4. Reconstructions on Real Solar Terminator region

[42] Figure 9 shows real TEC data, derived from MIDAS, for the ionosphere on an ordinary day, without any notable

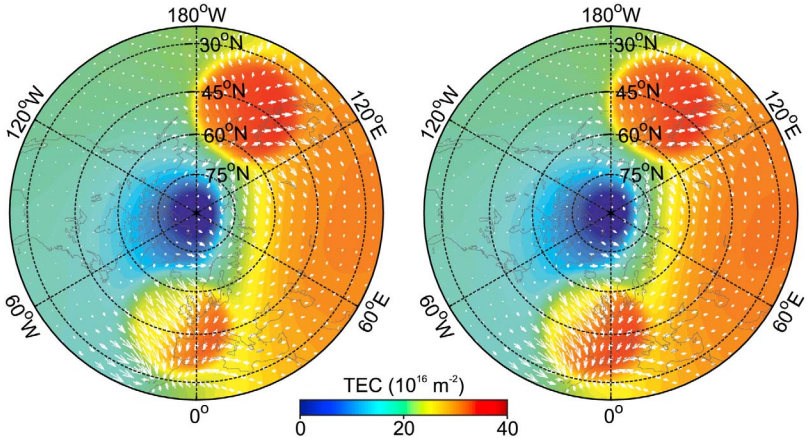

Figure 7. Demonstration of the solar terminator problem. Two objects, both moving away from the pole, are superimposed on a simulated ionospheric map: (left) first map and (right) second map. The calculated velocity arrows the same for both maps, and have been extended for clarity. Spurious motion is imparted onto both objects. Regularization parameters $r_v = 0.15$, $r_s = 0.5$ and $r_d = 0.5$ are used.

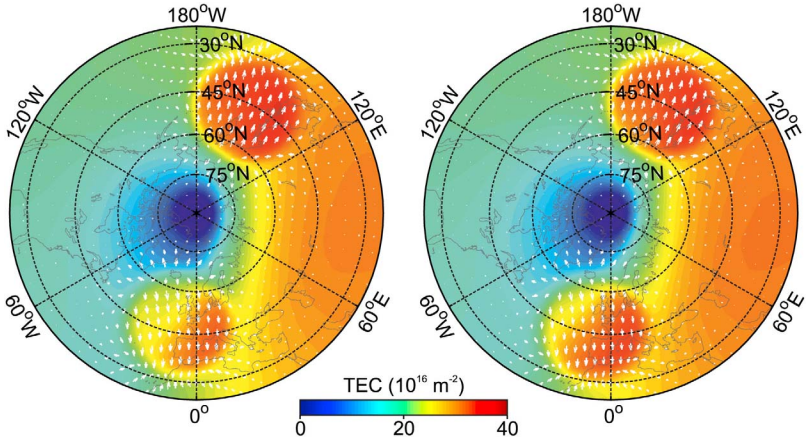

Figure 8. As for Figure 7, but with a source model added. The directions of the objects are correctly ascertained.

geomagnetic activity. Looking down from the north pole, a region of higher TEC appears to roughly move clockwise, corresponding to the sunlit region. The velocity reconstruction interprets the moving ionization gradient as being the movement of plasma in the solar terminator region.

[43] Figure 10 shows an attempt to correct for this by using the above source model. The velocity field is changed slightly, but the effect of apparent flow around the terminator region is not canceled out. This may be due to physical deficiencies in the model, and in particular, an inability to locate the boundary between regions of net ionization and net recombination to a great enough degree of accuracy. Resolving this deficiency is beyond the scope of this paper, but an outline of planned improvements to the model is given in Appendix A.

5. Conclusions

[44] The Horn-Schunck method for determining optical flow has been adapted to the problem of tracking the flow of plasma in the Earth's ionosphere. Given electron density fields at different times, the method finds the velocity field by inverting the continuity equation. The aperture problem was overcome by assuming irrotational flow with specified divergence to be the most pragmatic solution, but allowing deviations from this assumption to be made where needed.

[45] The method successfully reconstructed both test data and real ionospheric data, demonstrating that global optical flow techniques are potentially useful in studying the flow of plasma through the ionosphere. These reconstructions were achieved using a relatively light touch with respect to forcing the results to comply with models. The method can proceed automatically, and so is particularly suited to the analysis of data taken over extended time periods, where there may be thousands of different maps to be compared. This would allow statistical analysis of the correlation between plasma velocity and other phenomena to be performed. A future paper is planned, in which plasma velocity and the scintillation of GNSS signals is compared. A

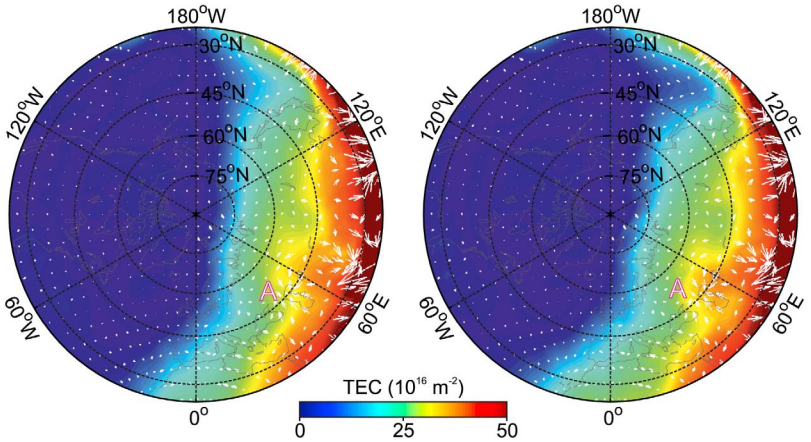

Figure 9. Demonstration of the solar terminator problem, on an ordinary day, without any notable geomagnetic activity showing (left) TEC at 07:30 UTC on October 28th 2011 and (right) TEC at 08:00 UTC. The calculated velocity arrows are the same for both maps, and have been extended for clarity. Over the Caspian Sea (A) plasma is assumed to rush into a patch that has almost certainly been created by photoionization. Regularization parameters $r_v = 0.15$, $r_s = 0.5$ and $r_d = 0.5$ are used.

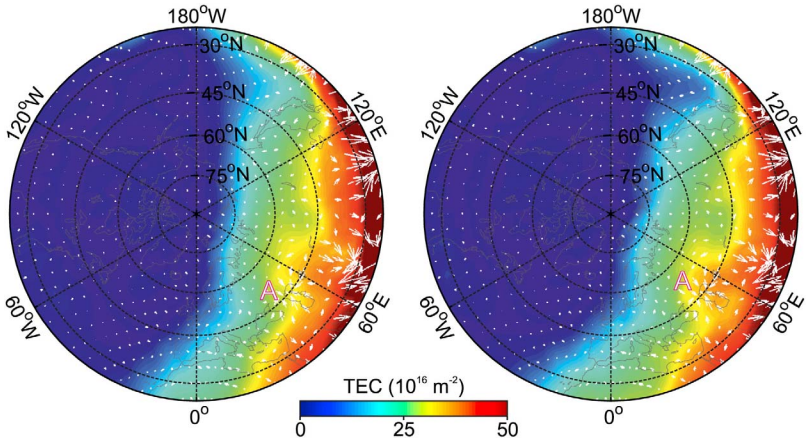

Figure 10. As for Figure 9, but with a model of plasma generation and recombination added to the reconstruction, in an attempt to correct for the solar terminator problem.

correlation between the two is known [*De Franceschi et al.*, 2007], but has only been studied for a relatively small number of isolated events. This paper will also include more rigorous testing of the method with real ionospheric data, and a study into the optimal combination of regularization parameters.

[46] The biggest problem so far is in compensating for solar terminator effects with models of plasma generation and recombination. To this end, the models used are still under development, and more advanced versions will be the subject of future publications. A more rigorous treatment of how inhomogeneities in the source term relate to the divergence of the plasma flow, will also be considered.

[47] Several other improvements could potentially be made to the reconstruction. One such improvement is to consider flow in three dimensions, rather than just two. This is straightforward mathematically, but would be problematic physically. Ionospheric maps generally have much poorer vertical resolution than horizontal resolution, plus the procedure would be complicated by the exchange of plasma between the plasmasphere and the ionosphere. Another possible upgrade is to add direct velocity component measurements from backscatter radar systems such as SuperDARN into the inversion. These are relatively sparse, but they would enhance the method, as they would introduce values unaffected by the aperture or solar terminator problems into the reconstruction. The modification could be made by adding an extra term to the energy functional integrand (equation (12)) penalizing deviations from the measured values.

Appendix A: Model of Generation and Recombination

[48] The model of generation and recombination in the ionosphere, as used in section 4.3, is described. The model is still under development, and in the simple form described here, lacks the accuracy to fully negate solar terminator effects.

[49] The model of photoionization was based on the EUV flux model for aeronomic calculations (EUVAC) [*Richards et al.*, 1994]. This splits the relevant region of the solar spectrum, from 1050Å extreme ultraviolet to 50Å soft X-ray, into a 37 element array. These elements either correspond to prominent emission lines, or to wavelength ranges. Absorption cross sections for the predominant neutral gases in the F-layer, O, O_2, N_2 were specified as a function of wavelength, using the same 37 element format [*Richards et al.*, 1994]. The densities of these gases were derived from the NRLMSISE-00 version of the Mass Spectrometer Incoherent Scatter (MSIS) empirical model [*Picone et al.*, 2002].

[50] Using this data, the attenuated solar spectrum at a given point in the atmosphere could be calculated by combining the attenuations over short increments of the raypath from the sun to the given point. Typically, 100 increments were used, starting from a 1000 km altitude. The attenuated solar spectrum could then be used to calculate the ionization rate by using ionization cross section data [*Richards et al.*, 1994]. This reference did not provide the difference between the absorption and ionization cross sections for O^+, and so it was augmented with data from *Fennelly and Torr* [1992].

[51] In the F-layer, O^+ ions account for the bulk of the plasma. This is produced by the ionization reaction

$$O \rightarrow O^+ + e^- \tag{A1}$$

The rate of direct recombination is negligible. Instead, recombination proceeds via the intermediate reactions

$$O^+ + O_2 \rightarrow O + O_2^+ \tag{A2}$$

$$O^+ + N_2 \rightarrow N + NO^+ \tag{A3}$$

$$O^+ + N_2 \rightarrow O + N_2^+ \tag{A4}$$

where the resulting O_2^+, NO^+ and N_2^+ decay via much faster reactions. The rate of these reactions depends on the neutral gas densities, as provided by MSIS, and known [*Torr and Torr*, 1979] rate coefficients. These coefficients are weakly dependent on ion temperature, and so a realistic estimate of

1000 K was used. At a given point in the ionosphere, the net rate of generation and recombination of O^+ ions, which is similar but not identical to that for electrons, is given by

$$s'_m = -\lambda\rho + \Gamma \quad \text{(A5)}$$

where Γ is the calculated rate of photoionization, and λ is the recombination coefficient. This in turn is given by

$$\lambda = \alpha[O_2] + \beta[N_2] \quad \text{(A6)}$$

where $[O_2]$ and $[N_2]$ are the concentration of these gases, α is the rate coefficient for reaction (A2), and β is the combined rate coefficient for reactions (A3) and (A4).

[52] A numerical issue arises when evaluating equation (A5), as ρ is itself dependent on s'_m. This is not important at high altitudes, but in the daytime F1 region, both Γ and $\lambda\rho$ can be very large and nearly identical, leaving s'_m as the slight difference between them. Therefore, the small error caused by the dependence of ρ on s'_m will introduce a large error to this critical difference. To resolve this problem, equation (A5) was first integrated over a time interval from t to $t + \Delta t$, giving

$$\rho = \rho_t e^{-\lambda\Delta t} + e^{-\lambda(t+\Delta t)} \int_{t'=t}^{t+\Delta t} \Gamma(t') e^{\lambda t'} dt' \quad \text{(A7)}$$

where the integration constant, ρ_t is the electron density at time t. This was then differentiated, to give an explicitly time dependent expression

$$s'_m = -\lambda\rho_t e^{-\lambda\Delta t} + \Gamma - \lambda e^{-\lambda(t+\Delta t)} \int_{t'=t}^{t+\Delta t} \Gamma(t') e^{\lambda t'} dt' \quad \text{(A8)}$$

which as expected, reduces to equation (A5) when $\Delta t = 0$. For the plasma flow calculation, Δt is equal to the time difference between maps. When evaluating equation (A8), the exponential within the integral can become very large, while the exponential outside the integral can become very small. If evaluated using standard floating-point computer arithmetic, the former quantity can overflow to infinity, and the latter quantity underflow to zero, giving an undefined answer. Therefore, when evaluating the functions, an integer offset value was subtracted from the argument of the inside exponential function, and the same value added to the argument of the outside exponential function, in order to prevent excessively large or small values. This integer was chosen to ensure that the highest exponential values were approximately one.

[53] To calculate the generation and recombination rate for free electrons, it is necessary to account also for O_2 and NO^+ ions. The former are produced by the photoionization described above, and by reaction (A2). The latter are produced by reaction (A3), and from the conversion of N_2^+ ions by the extremely rapid reaction

$$N_2^+ + O \rightarrow N + NO^+ \quad \text{(A9)}$$

where the N_2^+ ions are themselves are produced by reaction (A4) and by direct photoionization.

[54] The creation and destruction of O_2 and NO^+ ions occurs much more rapidly than variations in the O^+ density, and in the photoionization rates. Therefore, the densities of O_2 and NO^+ can be calculated by assuming that they are in equilibrium with the current O^+ density and photoionization rates. These equilibrium densities can be obtained by solving the equations

$$[O_2^+] = \alpha[O^+] + \Gamma_{O_2} - \zeta[e^-][O_2^+] \quad \text{(A10)}$$

$$[NO^+] = \beta[O^+] + \Gamma_{N_2} - \eta[e^-][NO^+] \quad \text{(A11)}$$

where ζ and η are the known [*Torr and Torr*, 1979] recombination rate coefficients for $[O_2^+]$ and $[NO^+]$ respectively. By plasma neutrality, the electron density $[e^-]$ is given by

$$[e^-] = [O^+] + [O_2^+] + [NO^+] \quad \text{(A12)}$$

By solving for $[O_2^+]$ and $[NO^+]$, and then adding their derivatives to s'_m, the rate of change of electron density s_m, could be calculated.

[55] In order to calculate the rate of change of electron density over a region in time, the electron density and the start of the interval, as needed for equation (A8), was calculated. This was done by starting from a value of zero, and then using equation (A7) to integrate over the previous 24 hours. For the 2D velocity reconstruction, s_m was integrated vertically, to give the change in TEC due to generation and recombination.

[56] The results differ from reality for several reasons. The most prominent failing is that although transport terms are necessarily removed when evaluating s, they should be present during the previous calculation of ρ_t. The chemistry model is also simplistic, as it ignores plasma temperatures, and also neglects the effects of excited states of the neutral gases. An upgraded model, taking these effects into account, will be the subject of future publications.

[57] **Acknowledgments.** The authors acknowledge financial support from the Engineering and Physical Sciences Research Council (EPSRC). To generate the ionospheric maps, we downloaded GPS data from the Crustal dynamics data information system, the École Nationale des Sciences Géographiques IGS service, the University NAVSTAR Consortium IGS service, and the University of California at San Diego Garner service.

[58] Robert Lysak thanks Gary Bust and another reviewer for their assistance in evaluating this paper.

References

Alexeev, I. I., E. S. Belenkaya, S. Y. Bobrovnikov, V. V. Kalegaev, J. A. Cumnock, and L. G. Blomberg (2007), Magnetopause mapping to the ionosphere for northward IMF, *Ann. Geophys.*, *25*, 2615–2625.

Barron, J. L., D. J. Fleet, and S. S. Beauchemin (1994), Performance of optical flow techniques, *Int. J. Comput. Vision*, *12*, 43–77.

Basu, S., and C. Valladares (1999), Global aspects of plasma structures, *J. Atmos. Sol. Terr. Phys.*, *61*, 127–139.

Basu, S., et al. (2001), Ionospheric effects of major magnetic storms during the international space weather period of September and October 1999: GPS observations, VHF/UHF scintillations, and in situ density structures at middle and equatorial latitudes, *J. Geophys. Res.*, *106*, 30,389–30,413.

Beauchemin, S. S., and J. L. Barron (1995), The computation of optical flow, *ACM Comput. Surv.*, *27*, 433–466.

Benyu, G., and C. Weiming (1995), A spectral method for the fluid flow with low Mach number on the spherical surface, *SIAM J. Numer. Anal.*, *32*, 1764–1777.

Bertero, M., T. A. Poggio, and V. Torre (1988), Ill-posed problems in early vision, *Proc. IEEE*, *76*, 869–889.

Bruhn, A., J. Weickert, and C. Schnorr (2005), Lucas/Kanade meets Horn/Schunck: Combining local and global optic flow methods, *Int. J. Comput. Vision*, *61*, 211–231.

Burston, R., I. Astin, C. Mitchell, L. Alfonsi, T. Pedersen, and S. Skone (2009), Correlation between scintillation indices and gradient drift wave amplitudes in the northern polar ionosphere, *J. Geophys. Res.*, *114*, A07309, doi:10.1029/2009JA014151.

Burston, R., K. Hodges, I. Astin, N. Bergeot, C. Bruyninx, and J. Chevalier (2010), Using ionospheric imaging combined with feature tracking to automate identification and tracking of polar-cap plasma patches, paper presented at 23rd International Technical Meeting, Satell. Div. of the Inst. of Navig., Portland, Oreg.

Bust, G., G. Crowley, N. Curtis, A. Reynolds, L. Paxton, C. Coker, and P. Bernhardt (2007), IDA4D—A new ionospheric imaging algorithm using non-linear ground-based and spaced-based data sources, *Eos Trans. AGU*, *88*(52), Fall Meet. Suppl., Abstract SA11B-06.

Bust, G. S., and G. Crowley (2007), Tracking of polar cap ionospheric patches using data assimilation, *J. Geophys. Res.*, *112*, A05307, doi:10.1029/2005JA011597.

Corpetti, T., E. Memin, and P. Perez (2002), Dense estimation of fluid flows, *IEEE Trans. Pattern Anal. Mach. Intell.*, *24*, 365–380.

Corpetti, T., D. Heitz, G. Arroyo, E. Memin, and A. Santa-Cruz (2006), Fluid experimental flow estimation based on an optical-flow scheme, *Exp. Fluids*, *40*, 80–97.

Datta-Barua, S., G. S. Bust, G. Crowley, and N. Curtis (2009), Neutral wind estimation from 4-D ionospheric electron density images, *J. Geophys. Res.*, *114*, A06317, doi:10.1029/2008JA014004.

Datta-Barua, S., G. S. Bust, and G. Crowley (2011), Deducing storm time *F* region ionospheric dynamics from 3-D time-varying imaging, *J. Geophys. Res.*, *116*, A05324, doi:10.1029/2010JA016304.

De Franceschi, G., L. Alfonsi, V. Romano, M. Aquino, A. Dodson, C. N. Mitchell, P. Spencer, and A. W. Wernik (2007), Dynamics of high-latitude patches and associated small-scale irregularities during the October and November 2003 storms, *J. Atmos. Sol. Terr. Phys.*, *70*, 879–888.

Doherty, P., A. J. Coster, and W. Murtagh (2004), Space weather effects of October–November 2003, *GPS Solutions*, *8*, 267–271.

Fennelly, J. A., and D. G. Torr (1992), Photioionization and photoabsorbtion cross sections of O, N_2, O_2 and N for aeronomic calculations, *Atom. Data Nucl. Data*, *51*, 312–363.

Fleet, D. J., and A. D. Jepson (1990), Computation of component image velocity from local phase information, *Int. J. Comput. Vision*, *5*, 77–104.

Foster, J. C., et al. (2005), Multiradar observations of the polar tongue of ionization, *J. Geophys. Res.*, *110*, A09S31, doi:10.1029/2004JA010928.

Foster, M. (2009), Reconstruction and motion estimation of sparsely sampled ionospheric data, PhD thesis, Univ. of Bath, Bath, U. K.

Foster, M. P., and A. N. Evans (2008), Segmentation and tracking of ionospheric storm enhancements, paper presented at XIVth Conference on Image and Signal Processing for Remote Sensing, Int. Soc. for Opt. and Photonics, Cardiff, U. K.

Foster, M. P., and A. N. Evans (2009), Tongue of ionization motion estimation from polar TEC sequences, *IEEE Geosci. Remote Sens. Lett.*, *6*, 582–586.

Gautama, T., and M. M. Van Hulle (2002), A phase-based approach to the estimation of the optical flow field using spatial filtering, *IEEE Trans. Neural Networks*, *13*, 1127–1136.

Horn, B. K. P., and B. G. Schunck (1981), Determining optical flow, *Artif. Intell.*, *17*, 185–203.

Imiya, A., H. Sugaya, A. Torii, and Y. Mochizuki (2005), Variational analysis of spherical images, in *Lecture Notes in Computer Science*, vol. 3691, pp. 104–111, Springer, Berlin.

Kinrade, J., C. N. Mitchell, P. Yin, N. Smith, M. J. Jarvis, D. J. Maxfield, M. C. Rose, G. S. Bust, and A. T. Weatherwax (2012), Ionospheric scintillation over Antarctica during the storm of 5–6 April 2010, *J. Geophys. Res.*, *117*, A05304, doi:10.1029/2011JA017073.

Klobuchar, J. A. (1996), Ionospheric effects on GPS, *Prog. Astronaut. Aeronaut.*, *163*, 485–515.

Lefèvre, J., and S. Baillet (2008), Optical flow and advection on 2-Riemannian manifolds: A common framework, *IEEE Trans. Pattern Anal. Mach. Intell.*, *30*, 1081–1092.

Lefèvre, J., G. Obozinski, and S. Baillet (2007), Imaging brain activation streams from optical flow computation on 2-Riemannian manifolds, *Inf. Process Med. Imaging*, *20*, 470–481.

Lucas, B. D., and T. Kanade (1981), An iterative image registration technique with an application to stereo vision, in *Proceedings of the 7th International Joint Conference on Artificial Intelligence*, edited by P. J. Hayes, pp. 674–679, William Kaufmann, Los Altos, Calif.

Mannucci, A. J., B. T. Tsurutani, B. A. Iijima, A. Komjathy, A. Saito, W. D. Gonzalez, F. L. Guarnieri, J. U. Kozyra, and R. Skoug (2005), Dayside global ionospheric response to the major interplanetary events of October 29–30, 2003 "Halloween storms," *Geophys. Res. Lett.*, *32*, L12S02, doi:10.1029/2004GL021467.

Middleton, H. R., S. E. Pryse, L. Kersley, G. S. Bust, E. J. Fremouw, J. A. Secan, and W. F. Denig (2005), Evidence for the tongue of ionization under northward interplanetary magnetic field conditions, *J. Geophys. Res.*, *110*, A07301, doi:10.1029/2004JA010800.

Mitchell, C. N., and P. S. J. Spencer (2003), A three-dimensional time-dependent algorithm for ionospheric imaging using GPS, *Ann. Geophys.*, *46*, 687–696.

Mitchell, C. N., L. Alfonsi, G. De Franceschi, M. Lester, V. Romano, and A. W. Wernik (2005), GPS TEC and scintillation measurements from the polar ionosphere during the October 2003 storm, *Geophys. Res. Lett.*, *32*, L12S03, doi:10.1029/2004GL021644.

Picone, J. M., A. E. Hedin, D. P. Drob, and A. C. Aikin (2002), NRLMSISE-00 empirical model of the atmosphere: Statistical comparisons and scientific issues, *J. Geophys. Res.*, *107*(A12), 1468, doi:10.1029/2002JA009430.

Richards, P. G., J. A. Fennelly, and D. G. Torr (1994), EUVAC: A solar EUV flux model for aeronomic calculations, *J. Geophys. Res.*, *99*, 8981–8992.

Rishbeth, H. (1986), On the F2-layer continuity equation, *J. Atmos. Terr. Phys.*, *48*, 511–519.

Skone, S., K. Knudsen, and M. de Jong (2001), Limitations in GPS receiver tracking performance under ionospheric scintillation conditions, in *Proceedings of the First COST Action 716 Workshop "Towards Operational GPS Meteorology" and the Second Network Workshop of the International GPS Service (IGS)*, vol. 26, pp. 613–621, Elsevier, New York.

Spencer, P. S. J., and C. N. Mitchell (2007), Imaging of fast moving electron-density structures in the polar cap, *Ann. Geophys.*, *50*, 427–434.

Stolle, C., J. Lilensten, S. Schlüter, C. Jacobi, M. Rietveld, and H. Lühr (2006), Observing the north polar ionosphere on 30 October 2003 by GPS imaging and IS radars, *Ann. Geophys.*, *24*, 107–113.

Suter, D. (1994), Motion estimation and vector splines, in *Proceedings CVPR'94: Computer Vision and Pattern Recognition*, pp. 939–942, Inst. of Electr. and Electron. Eng., Piscataway, N. J.

Tarantola, A. (2005), *Inverse Problem Theory and Model Parameter Estimation*, Soc. for Ind. and Appl. Math., Philadelphia, Pa.

Torr, D. G., and M. R. Torr (1979), Chemistry of the thermosphere and ionosphere, *J. Atmos. Terr. Phys.*, *41*, 797–839.

Tsurutani, B. T., et al. (2005), The October 28, 2003 extreme EUV solar flare and resultant extreme ionospheric effects: Comparison to other Halloween events and the Bastille Day event, *Geophys. Res. Lett.*, *32*, L03S09, doi:10.1029/2004GL021475.

Wildes, R. P., M. J. Amabile, A. Lanzillotto, and T. Leu (2000), Recovering estimates of fluid flow from image sequence data, *Comput. Vision Image Understanding*, *80*, 246–266.